



# Narrow optical linewidths and spin pumping on charge-tunable close-to-surface self-assembled quantum dots in an ultrathin diode

Matthias C. Löbl,<sup>1</sup> Immo Söllner,<sup>1</sup> Alisa Javadi,<sup>2</sup> Tommaso Pregnolato,<sup>2</sup> Rüdiger Schott,<sup>3</sup> Leonardo Midolo,<sup>2</sup> Andreas V. Kuhlmann,<sup>1,4</sup> Søren Stobbe,<sup>2</sup> Andreas D. Wieck,<sup>3</sup> Peter Lodahl,<sup>2</sup> Arne Ludwig,<sup>3</sup> and Richard J. Warburton<sup>1</sup>

<sup>1</sup>*Department of Physics, University of Basel, Klingelbergstrasse 82, CH-4056 Basel, Switzerland*

<sup>2</sup>*Niels Bohr Institute, University of Copenhagen, Blegdamsvej 17, Copenhagen DK-2100, Denmark*

<sup>3</sup>*Lehrstuhl für Angewandte Festkörperphysik, Ruhr-Universität Bochum, Universitätsstrasse 150, D-44780 Bochum, Germany*

<sup>4</sup>*IBM Research-Zurich, Säumerstrasse 4, 8803 Rüschlikon, Switzerland*

(Received 20 July 2017; revised manuscript received 10 October 2017; published 30 October 2017)

We demonstrate full charge control, narrow optical linewidths, and optical spin pumping on single self-assembled InGaAs quantum dots embedded in a 162.5-nm-thin diode structure. The quantum dots are just 88 nm from the top GaAs surface. We design and realize a  $p$ - $i$ - $n$ - $i$ - $n$  diode that allows single-electron charging of the quantum dots at close-to-zero applied bias. In operation, the current flow through the device is extremely small resulting in low noise. In resonance fluorescence, we measure optical linewidths below  $2 \mu\text{eV}$ , just a factor of 2 above the transform limit. Clear optical spin pumping is observed in a magnetic field of 0.5 T in the Faraday geometry. We present this design as ideal for securing the advantages of self-assembled quantum dots—highly coherent single-photon generation, ultrafast optical spin manipulation—in the thin diodes required in quantum nanophotonics and nanophononics applications.

DOI: [10.1103/PhysRevB.96.165440](https://doi.org/10.1103/PhysRevB.96.165440)

## I. INTRODUCTION

Single self-assembled quantum dots are a source of high quality single photons; they are also hosts for single spins [1–7]. Their large optical dipole moment enables fast initialization, manipulation, and readout of spin states all by optical means [2,6,8–10]. In the best case, transform-limited single-photon emission from single quantum dots has been demonstrated [11]. These properties are extremely sensitive to the quantum dot environment. The electrical environment can be controlled by embedding the quantum dots in diode heterostructures. This locks the Fermi energy and provides electrical control of the quantum dot charge state. Some of the best performances have been achieved in heterostructures that are  $\sim 500$  nm thick with the quantum dot positioned  $\sim 300$  nm from the GaAs-air interface [11,12].

The solid-state character of these emitters allows their optical [13] and mechanical [14,15] properties to be engineered by nanostructuring. For instance, embedding emitters in a membrane leads to the suppression of out-of-plane radiation modes through total internal reflection; control of the in-plane modes can be achieved via lateral patterning of the membrane. Cavities and waveguides can be engineered by creating defects in a photonic crystal band-gap structure. Single photons can be routed on a chip, and controlled by single two-level systems [16]. Likewise, engineering the mechanical properties can create phononic structures with the aim of controlling the quantum-dot-phonon interaction [14,15]. In all these applications, the basic building block is a thin GaAs membrane. It is crucial that the quantum dots in these thin structures exhibit the same excellent properties of quantum dots in bulklike structures. This has not been achieved so far.

Typical photonic crystal membranes, in the wavelength regime relevant for InGaAs quantum dots, range in total thickness from 120 to 200 nm [17,18]. Early demonstrations of charge control on quantum dots in photonic crystals used

thin  $p$ - $i$ - $n$  diode structures [18,19]. However, the large in-built electric field in combination with the small thickness of these devices led to a large potential at the position of the quantum dots shifting the Coulomb plateaus to large forward bias voltages. This resulted in high tunneling currents at the operating bias in  $p$ - $i$ - $n$ -membrane devices, a possible explanation for the absence of spin pumping in embedded quantum dots [18]. The quantum dot optical linewidths were relatively high in these structures.

In order to avoid the problems associated with high tunneling currents, we present here a quantum dot diode which operates close to zero bias. The main idea is to incorporate an  $n$ -layer within a  $p$ - $i$ - $n$  device, resulting in a  $p$ - $i$ - $n$ - $i$ - $n$  diode. The intermediate  $n$  layer is fully ionized. Most of the in-built field between the outer  $p$ - and  $n$ - gates drops between the top  $p$  gate and the intermediate  $n$  layer. The electric field at the location of the quantum dots is therefore much smaller than in a  $p$ - $i$ - $n$  diode with equal dimensions. This allows single-electron charging to occur close to zero bias. The  $p$ - $i$ - $n$ - $i$ - $n$  diode is used in silicon transistor technology [20,21], albeit with lateral rather than vertical control of the doping. It has also been employed in self-assembled quantum dot devices [19,22] but in these experiments narrow optical linewidths in combination with good spin properties were not achieved.

We present here a careful design which fulfills a list of criteria. The design rests on a full quantitative analysis of the band bending. It is realized using state-of-the-art GaAs heterostructures [11,23]. We present resonant laser spectroscopy on single quantum dots in a 162.5-nm-thick  $p$ - $i$ - $n$ - $i$ - $n$  diode with a quantum dot to surface distance of just 88 nm. Deterministic charge control at low bias, narrow optical linewidths, as well as optical spin pumping are demonstrated for these close-to-surface quantum dots. The developed heterostructure is ideal for electrical control of quantum dots in nanostructured membranes for photonic and phononic applications.

## II. *p-i-n-i-n* QUANTUM DOT HETEROSTRUCTURE

In the design of this structure we had to fulfill a number of constraints. First, the quantum dots should operate in the Coulomb blockade regime. This allows individual quantum dots to be loaded deterministically with single electrons. Within a Coulomb blockade plateau, the external bias allows some fine tuning of the optical transition frequencies via the dc Stark effect. Second, the dc current flowing through the device should be as small as possible to avoid decoherence processes. This can be guaranteed only if the charging voltage is close to zero bias. Third, the optical linewidths on driving the quantum dot resonantly should be small, close to the transform limit. This places stringent conditions on the level of charge noise that can be tolerated. Fourth, the membrane should have as little optical absorption as possible. Fifth, the membrane should be thinner than  $\sim 250$  nm to ensure single-mode behavior in waveguide structures. In fact, the fabrication of such nanostructures with a soft-mask technique sets a slightly stronger constraint: 180 nm is the maximum membrane thickness which can be processed with vertical sidewalls [24]. Sixth, the quantum dots must be located close to the center of the diode structure to maximize the coupling to TE-like photonic modes [13]. The combination the fifth and the sixth constraint means that the distance between quantum dots and surface cannot be more than 90 nm. Seventh, the spin relaxation time should be large so that the spin can be initialized and manipulated. In a diode device at low temperature, this means that the cotunneling rate between a quantum dot electron spin and the Fermi sea should be suppressed by using a relatively large tunnel barrier [25]. In such a situation, the spin can be initialized into one of its eigenstates by optical pumping [4,8,26,27].

Fulfilling these constraints is very challenging. It is clearly necessary to work with epitaxial gates, *n*- and *p*-type regions in the device, as a metallic Schottky barrier is highly absorbing. A thin *p-i-n* diode is in principle a possibility. However, at zero bias, there is a very large in-built electric field [Fig. 1(a)]. Furthermore, the quantum dots must be positioned at least 30–35 nm away from the *n*-type back contact in order to suppress cotunneling sufficiently. The combination of both constraints means that the quantum dot charges with a single electron only at a large and positive bias, around  $\sim 1$  V. Current flow through the device is inevitable under these conditions and high currents are hard to avoid [18,28]. The quantum dots could be located closer to the back gate while suppressing cotunneling by using AlGaAs tunneling barriers. Highly opaque AlGaAs tunneling barriers have been successfully used [29–31]. More transparent AlGaAs tunneling barriers require extremely precise control of thickness and Al content, hard to achieve in practice.

An alternative to the *p-i-n* diode is a diode with an additional *n* layer in the intrinsic region, a *p-i-n-i-n* device [Fig. 1(b)]. The additional *n* layer lies in the depletion region of the surrounding *p-i-n* diode. It is fully depleted such that it becomes positively charged. At zero bias, the total potential drop between *p*- and *n*- layers is the same as in the *p-i-n* diode, but now there is a large drop between the top *p* contact and

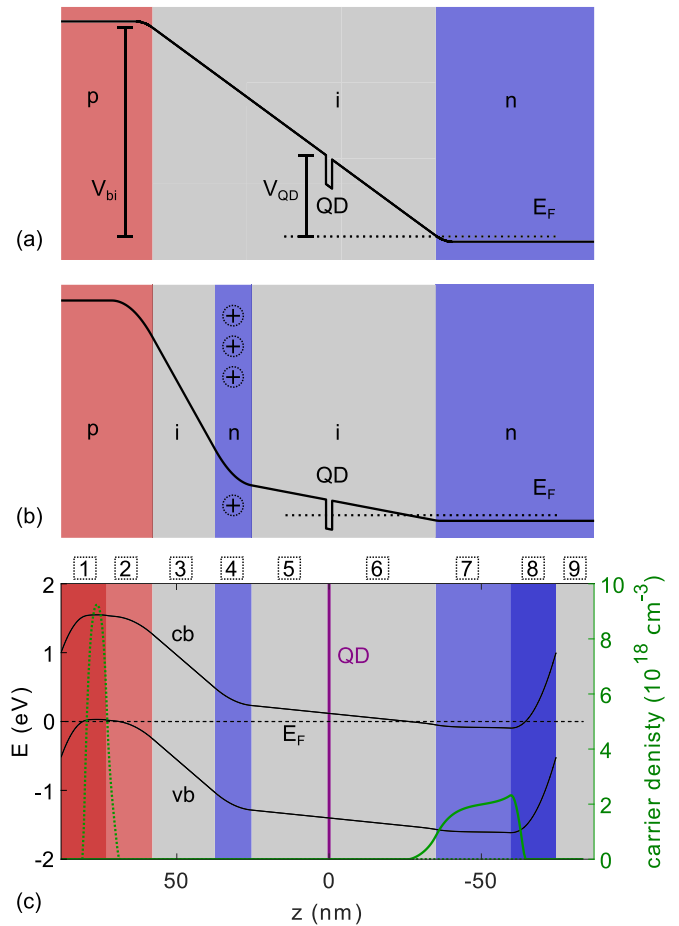


FIG. 1. (a),(b) Schematic conduction band profile of a *p-i-n* and *p-i-n-i-n* diode at zero bias voltage. In the *p-i-n-i-n* structure, an intermediate, fully ionized *n*-type layer causes band bending, reducing the potential difference between quantum dots and back gate. In this way, the quantum dots can be charged at a bias voltage close to zero. In contrast, a large positive voltage must be applied to the *p-i-n* diode. (c) Heterostructure of the investigated samples. Conduction- (cb) and valence- (vb) band edges are plotted in black and the density of free carriers is plotted in green (dotted line for holes, solid line for electrons). The dashed black line indicates the Fermi level  $E_F$ . The purple layer indicates the location of the quantum dots at the center of the membrane. The quantum dots are not included in the band-structure simulation. The diode structure is grown on top of a 1371-nm-thick  $\text{Al}_{0.75}\text{Ga}_{0.25}\text{As}$  sacrificial layer enabling selective underetching. The quantum dots are a distance of 35 nm away from a back gate consisting of two *n*-type layers (light and dark blue). The top gate consists of two *p*-type layers with different doping concentrations (indicated in red). An additional *n*-type layer is located between quantum dots and top gate. The full heterostructure is constructed as follows: 12.5 nm intrinsic GaAs (layer 9), 15 nm *n*-type GaAs with a doping concentration of  $n_{D+} = 8.0 \times 10^{18} \text{ cm}^{-3}$  (layer 8), 24.5 nm *n*-type GaAs with  $n_D = 2.0 \times 10^{18} \text{ cm}^{-3}$  (layer 7), 35 nm intrinsic GaAs (layer 6), a layer of InGaAs quantum dots, additional 25.5 nm intrinsic GaAs (layer 5), 12 nm *n*-type GaAs with  $n_d = 2.0 \times 10^{18} \text{ cm}^{-3}$  (layer 4), 20.5 nm intrinsic GaAs (layer 3), 15 nm *p*-type GaAs with  $n_A = 2.0 \times 10^{18} \text{ cm}^{-3}$  (layer 2), 15 nm *p*-type GaAs with  $n_{A+} = 1.0 \times 10^{19} \text{ cm}^{-3}$  (layer 1).



Plotted in Fig. 2(a) are the IV curves of the two samples, both showing diodelike behavior with very low tunneling currents for a large region around 0 V. This excellent electrical behavior is a consequence of both the high material quality of our wafers and the careful contacting of the  $p$  gate (see Appendix F). First tests of devices with nanostructures do not show an increased leakage current, but further investigations are required to rule out etched sidewalls as a possible source of increased leakage currents.

We characterize the charging behavior of a single quantum dot by measuring its photoluminescence (PL) as a function of an external bias voltage. Excitation is carried out with a continuous-wave laser with a wavelength of 830 nm (wetting layer excitation). The voltage applied between top and back gates of the sample changes the energy difference between the back gate Fermi level and the discrete energy levels of the quantum dot. The PL shows clear Coulomb blockade with a series of plateaus; see Fig. 2(c). We assign these plateaus to the neutral exciton  $X^0$  and the charged excitons  $X^{1-}$ ,  $X^{2-}$ , and  $X^{3-}$ . All charge plateaus appear in reverse bias, in a range between  $-0.7$  and  $-0.4$  V. At these bias voltages, the tunneling current through the sample is limited to only a few tens of nA for a mesa size of  $\sim 15$  nm<sup>2</sup> [see Fig. 2(b)], corresponding to a current density of less than  $\sim 3$  nA/mm<sup>2</sup>.

Our PL measurements can be interpreted in a majority-minority carrier picture: the optical excitation creates the minority carrier, the hole; the back gate provides majority carriers, electrons. For a 25 nm tunnel barrier (e.g., used in Refs. [12,25,33,34]), electron tunneling is typically much faster than recombination such that once a hole is captured, fast tunneling enables the exciton with the smallest energy to be formed before recombination occurs [10]. Abrupt changes in the PL spectrum as a function of bias result. In this work, the tunnel barrier is larger, 35 nm, and interpretation of the PL spectrum is slightly more involved.

In the first region of Fig. 2(c), the ground state is an empty quantum dot and the lowest energy excited state is  $X^0$ . When a single hole is captured by the quantum dot, it becomes energetically favorable for a single electron to tunnel into the quantum dot, forming an exciton and via recombination a photon at the  $X^0$  wavelength.

The first dashed line between regions 1 and 2 in Fig. 2(c) marks the point at which the  $X^{1-}$  and  $X^0$  energies cross, while the empty quantum dot remains the ground state of the system. In region 2, electrons begin to tunnel into the quantum dot once it has captured a single hole and the  $X^{1-}$  line appears. The fact that the  $X^0$  remains bright at this point, although not as bright as  $X^{1-}$ , indicates that the electron tunneling time into the quantum dot is comparable to the  $X^0$  radiative lifetime: recombination can occur before tunneling has created the exciton with lowest energy. We note that the tunneling rate is large enough that no quenching of the resonance fluorescence of  $X^{1-}$  due to an Auger process (by which an electron-hole pair in the  $X^{1-}$  decays by ejecting the second electron out of the quantum dot) is expected. The Auger process was demonstrated for thicker tunnel barriers [31].

Initially it is perhaps surprising that the  $X^0$  brightness increases in the regime where the quantum dot ground state is the single-electron state [region 3 of Fig. 2(c)]. These measurements are carried out in the weak excitation

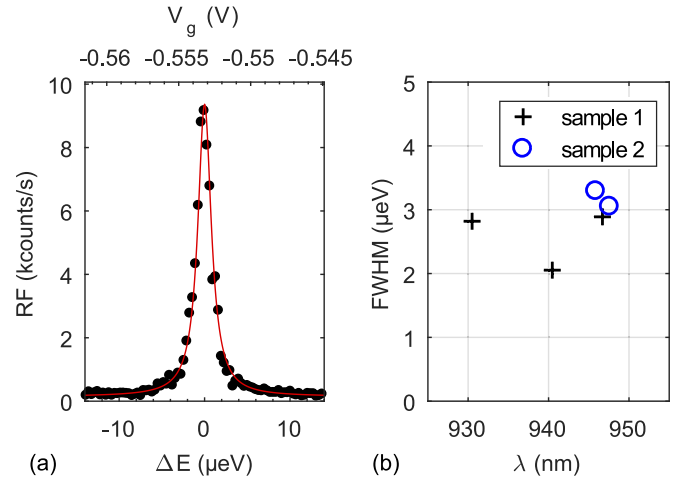


FIG. 3. (a) Resonance fluorescence of the singly charged exciton  $X^{1-}$  measured on the quantum dot shown in Fig. 2(b). The linewidth obtained by fitting a Lorentzian profile (red line) to the data (black circles) is  $1.9$   $\mu\text{eV}$  FWHM. The count rate is 22.5% of the saturation count rate. (b) Average linewidths across the singly charged exciton plateau for five quantum dots in two separate samples. The linewidths lie reproducibly in the range  $2$ – $3.5$   $\mu\text{eV}$ .

regime where hole capture is significantly slower than exciton recombination. The single-electron ground state implies that  $X^0$  recombination can take place as soon as a hole is captured. We speculate that the presence of an electron in the quantum dot increases the hole capture rate.

In the fourth region, the quantum dot is charged with two electrons in its ground state. Thus, capture of a single hole enables the  $X^{1-}$  recombination. In this region the intensity of  $X^0$  is small.  $X^{1-}$  recombination leaves behind a single electron. If a hole is captured before tunneling takes place,  $X^0$  emission is possible. However, this is unlikely with weak optical excitation (the case here) as electron tunneling is faster than hole capture.

Finally, in regions 5 and 6 the energetically favorable excitons are the  $X^{2-}$  and  $X^{3-}$  states. These states contain one and two electrons in the quantum-dot  $p$  shell, respectively. The tunneling barrier is more transparent for the  $p$  shell than for the  $s$  shell on account of the higher  $p$ -shell energy leading to faster tunneling times and therefore less overlap between the plateaus measured in PL.

The PL experiment establishes that the transition between the 0 and  $1e$  ground states takes place at  $-0.6$  V, not exactly at the design value of zero. This can be explained by a slight inaccuracy in the doping concentration of the intermediate  $n$ -type layer (see Appendix B). However, the flat IV characteristic in reversed bias implies that tunneling currents are still very small at this voltage. The measured IV characteristic is comparable to a  $p$ - $i$ - $n$  diode structure of similar thickness [18], but in the latter case charging would take place at large forward bias where tunneling currents are much bigger.

We turn now to resonant excitation of single quantum dots: this measures the exact optical linewidth. A resonance fluorescence (RF) measurement of the quantum dot presented in Fig. 2(b) is shown in Fig. 3(a). The resonant excitation

is carried out with a coherent, continuous-wave laser and the reflected laser light is suppressed with a cross-polarized detection scheme [32]. We make use of the Stark shift to sweep the quantum-dot transition through the resonance, using the applied bias voltage, while the excitation laser is kept at a constant wavelength. The measurement presented in Fig. 3(a) is carried out with a low excitation power corresponding to 22.5% of the saturation count rate. In the best case, linewidths below  $2 \mu\text{eV}$  (full width at half maximum, FWHM) are measured on second time scales. This performance is comparable to that of quantum dots in thick diode structures located far from the GaAs-air interface [11,12]. Narrow linewidths are reproducibly observed for different quantum dots in both samples [Fig. 3(b)]. Quantum dot linewidths are strongly influenced by charge noise. This measurement demonstrates forcibly that the level of charge noise in the close-to-surface, *p-i-n-i-n* device is similar to the ultralow charge noise in the very best far-from-surface, *p-i-n* device. Important for this low charge noise are screening of surface states in a gated structure [12] as well as very low tunneling currents at the operation point of the device.

## V. ELECTRON-SPIN PUMPING

Next we investigate the spin properties of a quantum dot by optical spin pumping experiments in a magnetic field in the Faraday geometry. The laser wavelength is changed stepwise to map the full Coulomb plateau. The background suppression of the dark-field microscope has a chromatic dependence and is therefore readjusted for each wavelength. In practice, this is carried out by an automatic algorithm which minimizes the intensity of the laser background by adjusting the polarization optics [32]. For a fixed laser wavelength the bias voltage is swept, sweeping the quantum dot transition with respect to the laser. This gives a “horizontal” cut through the  $X^{1-}$  exciton response; see Fig. 4(a). This procedure is repeated for different laser wavelengths giving a full map of the response over the single-electron Coulomb plateau. The results for zero magnetic field and a magnetic field of 0.5 T (Faraday geometry) are shown in Figs. 4(a) and 4(b), respectively. Both measurements are done with the same excitation power. In Fig. 4(b) the  $X^{1-}$  plateau shows a clear Zeeman splitting. Furthermore, the RF signal disappears in the middle of the plateau. This is the signature of optical spin pumping [26,27,35]: the spin is initialized in one of the spin eigenstates.

Spin pumping is interpreted in terms of the level scheme shown in Fig. 4(d). There are two strong transitions, the “vertical” transitions, and two weak transitions, the “diagonal” transitions. In the Faraday geometry, spin pumping arises due to the weakly allowed diagonal transitions in combination with a long electron-spin-relaxation time. On driving the  $|\uparrow\rangle \leftrightarrow |\uparrow\downarrow, \uparrow\rangle$  transition, the electron is pumped into the  $|\downarrow\rangle$  state via the weak diagonal transition  $|\uparrow\downarrow, \uparrow\rangle \leftrightarrow |\downarrow\rangle$  [green line in Fig. 4(d)]. The laser is no longer scattered by the quantum dot and the resonance fluorescence turns off. In the plateau center, the signal is reduced by a factor of  $\alpha_r = 40.1 \pm 1.6$  for the “red” transition, and by a factor of  $\alpha_b = 37.6 \pm 1.2$  for the “blue” transition, in both cases taking the RF intensity at zero magnetic field as reference. To quantify the spin initialization we estimate a spin initialization fidelity  $F = \sqrt{\langle \uparrow | \rho | \uparrow \rangle}$  for

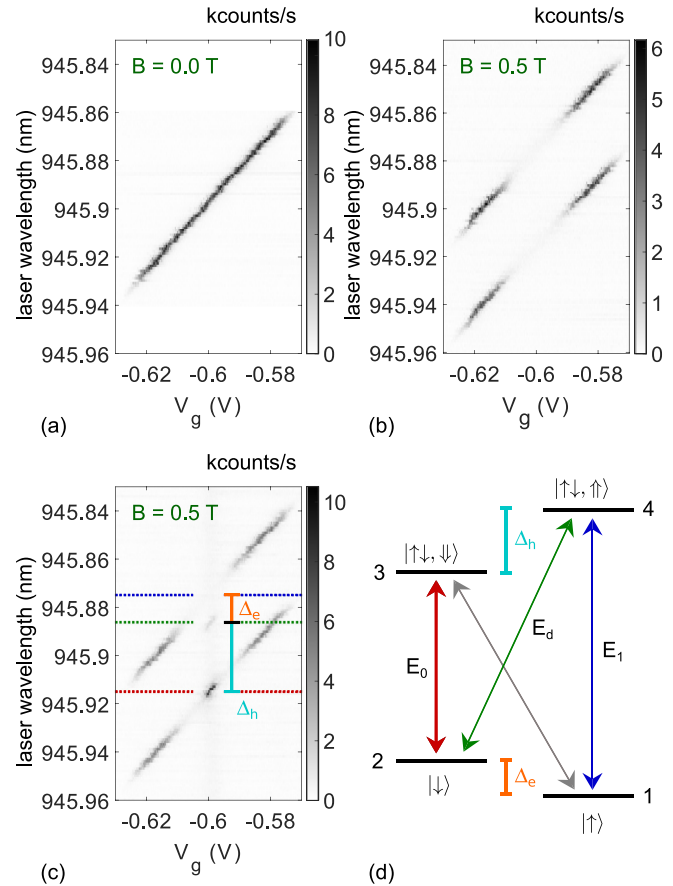


FIG. 4. (a) Resonance fluorescence of the singly charged exciton as a function of bias voltage and resonant laser wavelength. The measurement is carried out at zero external magnetic field on a quantum dot in sample 2. (b) RF of the same quantum dot at a magnetic field of  $B = 0.5 \text{ T}$  in the Faraday geometry. At the center of the plateau, the RF signal disappears due to optical spin pumping. (c) Resonant excitation is carried out with two lasers exciting the same quantum dot. The wavelength of the first laser is changed stepwise whereas the second laser is held at a constant wavelength of  $945.874 \text{ nm}$  (indicated by the blue line). The signal reappears when both vertical exciton transitions are excited simultaneously confirming the presence of optical spin pumping (indicated by the red line). When the second laser is in resonance with the diagonal transition  $|\downarrow\rangle \leftrightarrow |\uparrow\downarrow, \uparrow\rangle$  (indicated by the green line), the RF signal is also enhanced since the second laser pumps the quantum dot back to its bright transition  $|\uparrow\rangle \rightarrow |\uparrow\downarrow, \uparrow\rangle$ . However, this enhancement is weaker, since the corresponding transition is dipole “forbidden”, i.e., only weakly allowed. The observation of the diagonal transition allows the Zeeman splittings,  $\Delta_e$  and  $\Delta_h$  for electron and hole, respectively, to be determined. Note that in (a)–(c) all lasers are kept at the same power. (d) Level scheme of the quantum dot in the Faraday geometry.

pumping the red, and  $F = \sqrt{\langle \downarrow | \rho | \downarrow \rangle}$  for the blue transition. The initialization fidelity can be related to the resonance fluorescence via  $F = \sqrt{1 - 1/\alpha_{r/b}}$  (see Appendix D for details). This way we estimate initialization fidelities of  $F = 98.7\%$  for both spins. A significant difference is not expected at 4.2 K and small magnetic fields as the thermal energy is much larger than the Zeeman splitting between the electron-spin states. At

the edges of the one-electron Coulomb plateau, the RF signal does not disappear. At the plateau edges, cotunneling with the Fermi sea in the back gate randomizes the spin rapidly and spin pumping becomes ineffective [25]. The observation of optical spin pumping in the Faraday geometry confirms that the spin-flip processes which couple the two electron-spin states  $|\uparrow\rangle, |\downarrow\rangle$  are significantly slower than the decay rate of the weakly allowed diagonal transition [27].

To confirm that the observed disappearance of the signal arises due to optical spin pumping, we repeat the experiment with a second laser, a repump laser [26]. The second laser has a fixed wavelength of 945.87 nm, the wavelength of the vertical transition  $|\uparrow\rangle \leftrightarrow |\uparrow\downarrow, \uparrow\rangle$  [blue arrow in Fig. 4(d)]. These measurements are shown in Fig. 4(c). The laser powers are kept constant throughout the entire scan. Two repump resonances are observed [marked by red and green dashed lines in Fig. 4(d)].

When the first laser, the “pump” laser, is in resonance with the vertical transition  $|\downarrow\rangle \leftrightarrow |\uparrow\downarrow, \downarrow\rangle$ , the electron spin is shelved in the  $|\uparrow\rangle$  state and with this laser alone, the RF disappears. However, in the presence of the repump laser, the electron spin is driven back into the  $|\downarrow\rangle$  state and the RF reappears: the electron spin ends up in a statistical mixture of the two spin states. Similarly, the system ends up in a mixture of the spin states when the pump laser is stepped into resonance with the weakly allowed diagonal transition  $|\downarrow\rangle \leftrightarrow |\uparrow\downarrow, \uparrow\rangle$ . However, since the diagonal transition is only weakly allowed, the RF is relatively weak in this case. These observations explain the origin and intensity of the two repump resonances.

The fact that the diagonal transition  $|\downarrow\rangle \rightarrow |\uparrow\downarrow, \uparrow\rangle$  is visible allows the energies of all three optical transitions to be determined. The energies of the different exciton transitions are denoted as  $E_1$  for the transition  $|\uparrow\rangle \rightarrow |\uparrow\downarrow, \uparrow\rangle$ ,  $E_0$  for  $|\downarrow\rangle \rightarrow |\uparrow\downarrow, \downarrow\rangle$ , and  $E_d$  for  $|\downarrow\rangle \rightarrow |\uparrow\downarrow, \uparrow\rangle$  [see Fig. 4(d)]. The electron and hole Zeeman splitting are given by  $\Delta_e = E_1 - E_d$  and  $\Delta_h = E_d - E_0$ . This allows the magnitude of the electron and hole  $g$ -factors to be determined via the relations  $\Delta_{e/h} = g_{e/h}\mu_B B$ . Assuming that the electron  $g$ -factor is negative, we find an electron  $g$ -factor of  $g_e = -0.55$  and a hole  $g$ -factor of  $g_h = 1.37$ , values comparable to those in the literature [18,26,36].

## VI. CONCLUSIONS

In conclusion, we have designed a  $p$ - $i$ - $n$ - $i$ - $n$  diode structure with a thickness of just 162.5 nm. The device enables single electron charging of embedded self-assembled quantum dots at low bias voltage and with small tunneling currents. The diode is fully compatible with the fabrication of photonic and phononic nanostructures in thin membranes. We demonstrate narrow optical linewidths and optical spin pumping for the close-to-surface quantum dots in the  $p$ - $i$ - $n$ - $i$ - $n$  diode. These excellent properties will underpin future exploitations of quantum dot spins in functionalized nanostructures.

## ACKNOWLEDGMENTS

M.C.L., I.S., A.V.K., and R.J.W. acknowledge financial support from NCCR QSIT and from SNF Project No. 200020\_156637. This project has received funding from

the European Unions Horizon 2020 research and innovation program under Marie Skłodowska-Curie Grant Agreement No. 747866 (EPPIC). A.J., T.P., L.M., S.S., and P.L. gratefully acknowledge financial support from the European Research Council (ERC Advanced Grant “SCALE”), Innovation Fund Denmark (Quantum Innovation Center “Qubiz”), and the Danish Council for Independent Research. S.S. acknowledges Villum Fonden for financial support. R.S., A.L., A.D.W. gratefully acknowledge financial support from Grants No. DFH/UFA CDFA05-06, No. DFG TRR160, and No. BMBF Q.com-H 16KIS0109.

## APPENDIX A: ANALYTICAL BAND-STRUCTURE MODEL

We present an analytic calculation of the band structure of the  $p$ - $i$ - $n$ - $i$ - $n$  diode [21]. To this end, we divide the heterostructure in five different regions (Fig. 5). The first region (A) is the depletion zone of the  $p$ -type top gate, of width  $w_p$  and doping concentration  $n_A$ , part of layer number 2 in Fig. 1(c). The second region (B) is the intrinsic GaAs layer between top gate and an intermediate  $n$  layer [layer 3 in Fig. 1(c)]. Its width is denoted by  $L_1$ . The third region (C) is the intermediate  $n$  layer [layer 4 in Fig. 1(c)] with a width denoted by  $w$  and doping concentration  $n_d$ . The fourth region (D) is the subsequent intrinsic region of width  $L_2$  which includes the quantum dot layer [layer 5, 6 in Fig. 1(c)]. The final region (E) is the depletion zone of the back gate [part of layer 7 in Fig. 1(c)]. It has a width of  $w_n$  and a doping concentration of  $n_D$ .

We apply the Poisson equation  $\Delta\Phi = -\frac{e\cdot n}{\epsilon\epsilon_0}$  to all five regions ( $e$  electron charge,  $\epsilon_0$  vacuum permittivity,  $\epsilon$  relative permittivity of GaAs, and  $n$  carrier density). Note that the potential  $\Phi$  is defined for a positive probe charge and has to be reversed in sign to describe an electron in the conduction band. Together with the constraints that the electric displacement field  $-\epsilon\epsilon_0\frac{\partial\Phi}{\partial z}$  must be continuous and vanishes at the outer edges of the depletion zones, one obtains the following five equations for the electric field in the different regions A–E of the structure:

$$\text{A : } \frac{\partial\Phi}{\partial z} = \frac{e}{\epsilon\epsilon_0}n_A(z + w_p + L_1), \quad (\text{A1})$$

$$\text{B : } \frac{\partial\Phi}{\partial z} = \frac{e}{\epsilon\epsilon_0}n_Aw_p, \quad (\text{A2})$$

$$\text{C : } \frac{\partial\Phi}{\partial z} = \frac{e}{\epsilon\epsilon_0}(n_Aw_p - n_dz), \quad (\text{A3})$$

$$\text{D : } \frac{\partial\Phi}{\partial z} = \frac{e}{\epsilon\epsilon_0}(n_Aw_p - n_dw), \quad (\text{A4})$$

$$\text{E : } \frac{\partial\Phi}{\partial z} = \frac{e}{\epsilon\epsilon_0}[n_D(L_2 + w - z) + n_Aw_p - n_dw]. \quad (\text{A5})$$

Integration of the electric field in all five regions of the diode yields the potential drop  $\Delta V$  between top gate and back gate:

$$\begin{aligned} \frac{\epsilon\epsilon_0}{e}\Delta V &= \frac{\epsilon\epsilon_0}{e}(V_0 - V_{\text{bias}}) \\ &= \frac{n_A}{2}w_p^2 + n_Aw_pL_1 + n_Aw_pw - \frac{n_d}{2}w^2 \\ &\quad + L_2(n_Aw_p - n_dw) - \frac{n_D}{2}w_n^2 \\ &\quad + w_n(n_Aw_p - n_dw), \end{aligned} \quad (\text{A6})$$

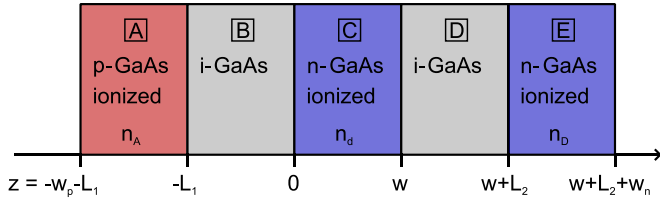


FIG. 5. Schematic *p-i-n-i-n* diode with labels used in the analytical calculation of the band structure. The letters (A–E) in the frames correspond to the different regions considered in the band-structure calculation; the colors indicate the corresponding layers of the diode shown in Fig. 1(c).

where  $V_0$  is the in-built voltage of the diode and  $V_{\text{bias}}$  is the externally applied bias voltage. For high doping concentrations when top and back gate are degenerately doped, the in-built voltage is given by  $eV_0 = E_{\text{gap}} + E_{\text{F}}^e + E_{\text{F}}^h$  where  $E_{\text{gap}}$  is the band gap of GaAs and  $E_{\text{F}}^{e/h}$  is the Fermi level for electrons in the back gate and holes in the top gate, respectively [ $E_{\text{F}}^{e/h} = \hbar^2/2m_{e/h}^*(3\pi^2n)^{2/3}$ ]. The condition that the entire device is charge neutral,

$$-n_A w_p + n_d w + n_D w_n = 0, \quad (\text{A7})$$

in combination with Eq. (A6), determines the widths of the depletion zones  $w_p$  and  $w_n$ :

$$\begin{aligned} w_p &= \frac{1}{a_1} \left( a_2 + \sqrt{a_2^2 + 2a_1 a_3} \right), \quad a_1 = n_A + \frac{n_A^2}{n_D}, \\ a_2 &= -n_A L_2 - n_A w - n_A L_1 + \frac{n_A n_d}{n_D} w, \\ a_3 &= n_d L_2 w + \frac{n_d w^2}{2} + \frac{\epsilon \epsilon_0}{e} \Delta V - \frac{n_d^2 w^2}{2n_D}, \\ w_n &= \frac{1}{n_D} (n_A w_p - n_d w). \end{aligned} \quad (\text{A8})$$

Using Eq. (A8) the potential as a function of vertical position inside the heterostructure is obtained by integration over Eqs. (A1)–(A5). In particular, the electric field at the position of a quantum dot is given by Eq. (A4).

## APPENDIX B: BIAS VOLTAGE OF COULOMB PLATEAUS

We present a possible explanation for the fact that the 0-1 electron transition takes place at a bias voltage of  $V_{\text{bias}} = -0.6$  V and not around zero bias as intended. Deviations of heterostructure or quantum dot parameters can shift this transition voltage. The part of the heterostructure that influences the 0-1e transition voltage most strongly is the intermediate *n*-type layer. A deviation in its thickness or its doping concentration can change the electric field experienced by the quantum dot. The layer thickness can be controlled rather precisely in MBE growth and we thus simulate the 0-1e transition voltage as a function of the doping concentration of the intermediate *n* layer. The ratio between doping of the intermediate *n* layer and doping of the back gate is kept constant for this estimation since a systematically different *n* doping would affect both layers. We use the analytical model and also numerical band-structure simulations (nextnano). We take a single electron

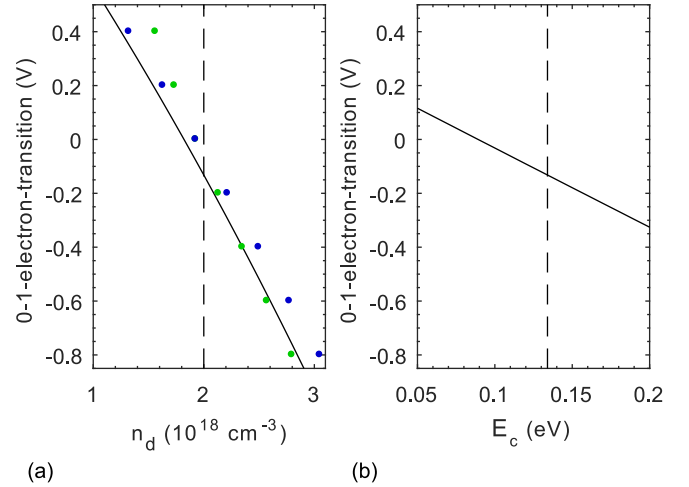


FIG. 6. (a) Calculated shift of the 0-1 electron charging transition as a function of the doping of the intermediate *n*-type layer  $n_d$ . The back gate doping is scaled correspondingly ( $n_d = n_D$ ). The black curve shows the result of the analytical calculation (see Appendix A); the green points represent the results of band-structure simulations including surface depletion; the blue points represent the results of band-structure simulations assuming ohmic contacts. (b) Shift of the 0-1 electron charging transition as a function of the single electron confinement energy  $E_c$ .

confinement energy of the quantum dot of  $E_c = 134$  meV [37] and vary the doping concentration [Fig. 6(a)]. The 0-1 electron transition voltage obtained numerically assuming ohmic boundary conditions agrees well with the analytical model, but is systematically slightly larger. We explain this by the fact that the numerical Poisson equation solver takes into account a charge overspill of back gate electrons into the intrinsic region [see Fig. 1(c)]. This effect lifts the conduction-band energy slightly at the location of the QDs. In contrast the analytical model assumes abrupt depletion regions. A numerical simulation taking into account surface depletion via Schottky barriers of 1 V gives comparable results (see Fig. 6). Surface effects are not considered in the analytical model. All this work predicts a 0-1e transition voltage of about  $-0.1$  V for the nominal doping concentration  $n_d = 2.0 \times 10^{18} \text{ cm}^{-3}$ .

Figure 6(b) shows the 0-1 electron transition voltage as a function of the quantum dot single electron confinement energy  $E_c$  keeping the doping at the nominal value of  $n_d = 2.0 \times 10^{18} \text{ cm}^{-3}$ . The dashed black line indicates a single electron confinement energy of  $E_c = 134$  meV that has been reported in the literature [37]. One can see that the shift of the 0-1e transition voltage to  $-0.6$  V cannot be explained by any realistic single electron confinement potential of the quantum dot. This suggests that the most likely explanation for the shift of the 0-1e transition to  $-0.6$  V is a deviation of the *n* doping from the nominal value. An increase by about 30% reproduces the experimental result taking  $E_c = 134$  meV [Fig. 6(a)]. A reduced doping of the *p*-type top gate would also shift the 0-1e transition to more negative bias voltages. However, the effect of an underdoped *p* layer is smaller and cannot explain the shift to  $-0.6$  V completely.

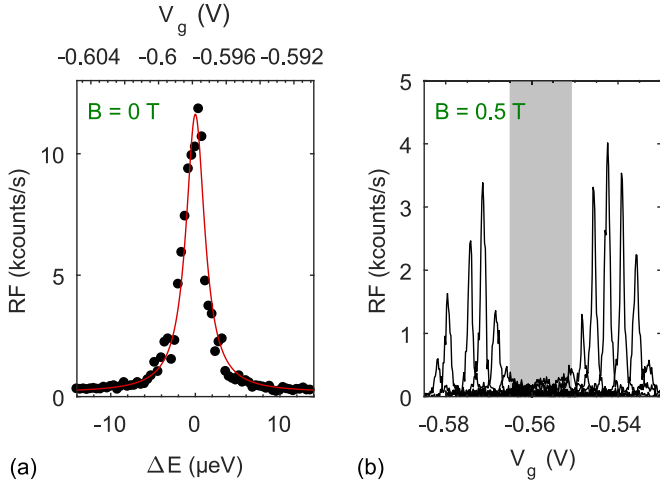


FIG. 7. (a) Resonance fluorescence of a quantum dot in sample 2 (the one from Fig. 4). The linewidth obtained by a Lorentzian fit (red curve) is  $2.7 \mu\text{eV}$  for a power corresponding to 27% of the saturation count rate. (b) Optical spin pumping on the singly charged exciton for a quantum dot in sample 1 (the one from Fig. 3) at a magnetic field of 0.5 T. The different peaks correspond to RF measurements for different excitation wavelengths. The gray shaded region indicates the regime where the spin pumping dominates over cotunneling processes and the RF signal thus disappears. At the plateau edges, the cotunneling dominates and resonance fluorescence reappears.

#### APPENDIX C: SUPPLEMENTARY EXPERIMENTAL DATA

In the main text, we presented narrow linewidths for a quantum dot in sample 1 whereas optical spin pumping is demonstrated for a quantum dot in sample 2. To illustrate that our measurements are reproducible on different quantum dots, we show in Fig. 7 a typical linewidth for the quantum dot in sample 2, and demonstrate optical spin pumping for the quantum dot in sample 1.

#### APPENDIX D: ANALYSIS OF SPIN PUMPING

Here we show how resonance fluorescence of the singly charged exciton is used to obtain spin initialization fidelities. In Sec. V, the initialization fidelity was connected to the ratio  $\alpha_{r/b}$  between the RF intensity when no spin pumping is present (at  $B = 0$  T) and the RF intensity when spin pumping is active (at  $B = 0.5$  T).

We give a derivation of this relation in a rate-equation picture. At zero magnetic field, both allowed transitions  $|\downarrow\rangle \leftrightarrow |\uparrow\downarrow, \downarrow\rangle$  and  $|\uparrow\rangle \leftrightarrow |\uparrow\downarrow, \uparrow\rangle$  are degenerate [see Fig. 4(d)]. In the steady state, the ratio between occupation of upper and lower levels is given by

$$\frac{N_3^{B=0}}{N_2^{B=0}} = \frac{N_4^{B=0}}{N_1^{B=0}} = \frac{\Gamma}{\Gamma + \gamma + \gamma_D} \equiv b \quad (\text{D1})$$

with  $N_3^{B=0} = N_4^{B=0}$  the occupation of the excited states and  $N_2^{B=0} = N_1^{B=0}$  the occupation of the ground states [see Fig. 4(d) for labels].  $\Gamma$  denotes the stimulated emission/excitation rate,  $\gamma$  the spontaneous emission rate via the dipole-allowed vertical transitions, and  $\gamma_D$  the spontaneous emission rate via the diagonal transitions. The resonance

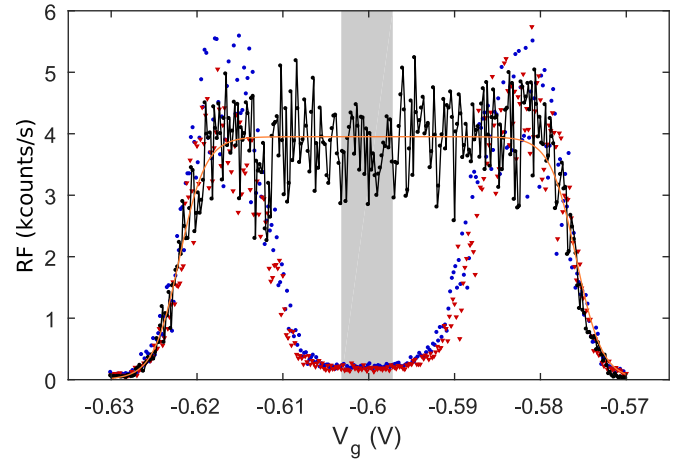


FIG. 8. Resonance fluorescence intensity along the single electron Coulomb plateau for the quantum dot shown in Fig. 4. The black curve shows data at 0.0 T divided by a factor of 2 (to give a signal per spin); the red triangles (blue circles) show the data at 0.5 T for the lower (higher) frequency Zeeman transitions. To obtain the ratio between the plateau intensities with and without spin pumping, the corresponding signals are averaged in the plateau center (gray shaded region). The orange curve is a fit of the data at  $B = 0.0$  T to Eq. (E1).

fluorescence intensity  $\text{RF}^{B=0}$  is directly connected to the occupation of the upper states:  $\text{RF}^{B=0} = \tilde{c}(N_3^{B=0} + N_4^{B=0})$ . The combination of Eq. (D1) and the normalization condition  $\sum_{i=1}^4 N_i^{B=0} = 1$  yields the equation

$$\text{RF}^{B=0} = \tilde{c}(N_3^{B=0} + N_4^{B=0}) = \frac{\tilde{c}}{1+b}. \quad (\text{D2})$$

In finite magnetic field, the transitions  $|\downarrow\rangle \leftrightarrow |\uparrow\downarrow, \downarrow\rangle$  and  $|\uparrow\rangle \leftrightarrow |\uparrow\downarrow, \uparrow\rangle$  are split in energy. We take the case when the redshifted transition  $|\downarrow\rangle \leftrightarrow |\uparrow\downarrow, \downarrow\rangle$  is driven by a laser field whereas the other one is not addressed. This means that  $N_4^{B \neq 0} = 0$  and the resonance fluorescence is connected to the occupation of just one upper level:  $\text{RF}^{B \neq 0} = \tilde{c}N_3^{B \neq 0}$ . In the steady state, the ratio of  $N_3^{B \neq 0}$  and  $N_2^{B \neq 0}$  is also given by the relation  $N_3^{B \neq 0}/N_2^{B \neq 0} = b$ ; see Eq. (D1). In combination with the normalization condition  $\sum_{i=1}^3 N_i^{B \neq 0} = 1$  this leads to

$$\text{RF}^{B \neq 0} = \tilde{c}N_3^{B \neq 0} = \tilde{c} \frac{1 - N_1^{B \neq 0}}{1+b}. \quad (\text{D3})$$

The combination of Eqs. (D2) and (D3) directly connects the occupation  $N_1^{B \neq 0}$  of the ground state with the resonance fluorescence intensities:

$$N_1^{B \neq 0} = 1 - \frac{1}{\alpha_r}, \quad \text{with } \alpha_r = \frac{\text{RF}^{B=0}}{\text{RF}^{B \neq 0}}. \quad (\text{D4})$$

This equation shows how the initialization fidelity can be deduced from the RF measurements.

The corresponding values of  $\alpha_{r/b}$  are determined in the following way. For every bias voltage, the maximum RF signal (Fig. 4) is determined. Results are plotted in Fig. 8 for the two transitions at 0.5 T (Zeeman split) and for the single transition at zero magnetic field. The signals are averaged over a small region in the Coulomb plateau center to determine

accurately the strength of the resonance fluorescence in the regime where optical spin pumping dominates over spin cotunneling. In this way, we determine the intensity ratio  $\alpha_{r/b}$  between the signal at zero magnetic field and the signal at  $B = 0.5$  T.

#### APPENDIX E: LEVER ARM APPROXIMATION

On increasing the bias voltage from the center of the Coulomb plateau, the  $X^{1-}$  RF drops once it becomes electrically favorable for a second electron to tunnel into the quantum dot. On the other hand, on decreasing the bias voltage from the plateau center, the  $X^{1-}$  RF drops once it becomes energetically favorable for the electron to tunnel out of the quantum dot. In both cases, the edges of the  $X^{1-}$  plateau are not abrupt since the electron occupation in the back gate is determined by a thermally smeared Fermi distribution. At its edges, the  $X^{1-}$  RF signal maps the Fermi distribution of the back gate and is well described by a two-sided Fermi distribution:

$$I_{\text{RF}}(V) = I_0 \frac{1}{1 + \exp\left(\frac{e(V-V_1)}{\lambda_{\text{diff}} k_B T}\right)} \times \frac{1}{1 + \exp\left(\frac{e(V_2-V)}{\lambda_{\text{diff}} k_B T}\right)}, \quad (\text{E1})$$

where  $k_B T$  is the thermal energy,  $V_1$  and  $V_2$  specify the bias voltage at the plateau edges, and  $I_0$  is the intensity in the plateau center. The variable  $\lambda_{\text{diff}}$ , the differential lever arm, is defined by  $\lambda_{\text{diff}} = e\left(\frac{\partial \Phi_{\text{QD}}}{\partial V_{\text{bias}}}\right)^{-1}$  where  $\Phi_{\text{QD}}$  is the energy difference between back gate Fermi energy and the quantum dot single electron level. Thus,  $\lambda_{\text{diff}}$  parametrizes how the potential of the quantum dot changes with bias voltage  $V_{\text{bias}}$ .

We determined the differential lever arm as a function of the bias voltage by using numerical band-structure simulations. We find a value of  $\lambda_{\text{diff}} = 4.17$  at a bias voltage of  $-0.6$  V. A slightly increased  $n$  doping explaining the  $0-1e$  transition at this bias is taken into account (see Appendix B). In the simulation, the lever arm is to a good approximation constant over the single electron Coulomb plateau. We fit the model described by Eq. (E1) using the position of the plateau edges  $V_1$  and  $V_2$  and the plateau intensity  $I_0$  as the only fit parameters. The temperature 4.2 K as well as the differential lever arm are fixed parameters in the fit. The fit describes the experimental data very well (Fig. 8). This is further evidence that the electrical properties of our sample are well understood.

As a final remark we note that often the lever arm is also defined as  $\lambda_{\text{geo}} = L/L_{\text{QD}}$  (geometrical lever arm) and  $\lambda_{\text{el}} = e\left(\frac{\partial \Phi_{\text{QD}}}{\partial V_0 - V_{\text{bias}}}\right)^{-1}$  (electrical lever arm). For diode structures with little band bending, the three parameters  $\lambda_{\text{diff}}$ ,  $\lambda_{\text{el}}$ , and  $\lambda_{\text{geo}}$  are to a good approximation equivalent [25,27,38]. Obviously,

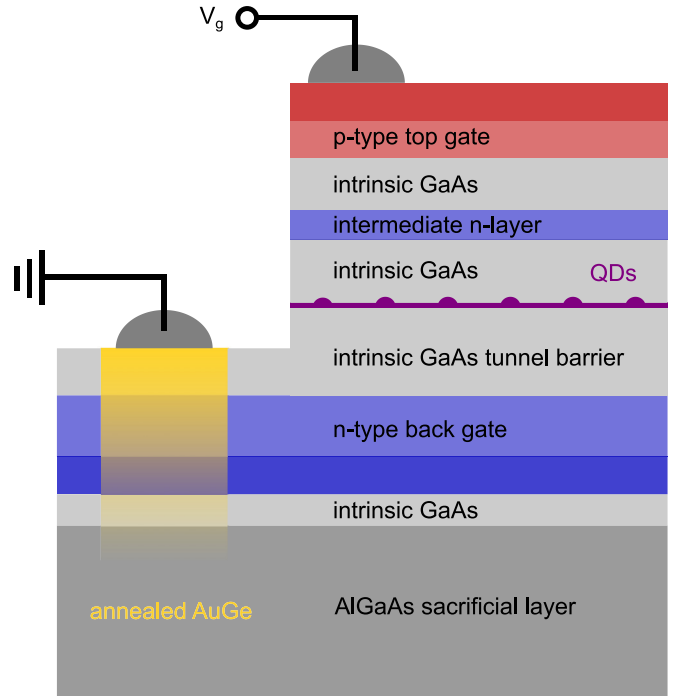


FIG. 9. Schematic of the sample. In order to make electrical contacts, the top gate is removed in part of the sample by wet chemical etching. An AuGe contact (yellow) is annealed into the back gate. Both top and back gate are contacted with silver paint.

this is not the case for the heterostructure presented here as a result of band bending in the  $p-i-n-i-n$  structure.

#### APPENDIX F: SAMPLE FABRICATION

To fabricate devices from the wafer material, first a mesa structure is defined by means of optical lithography. The top gate is etched away around this mesa so that an independent contact to the back gate can be made. A wet chemical process with a diluted mixture of sulfuric acid and hydrogen peroxide (1  $\text{H}_2\text{SO}_4$  : 1  $\text{H}_2\text{O}_2$  : 50  $\text{H}_2\text{O}$ ) was used for the etching. Subsequently, a contact pad of Au/Ge/Ni is evaporated onto the new etched surface and then annealed at  $420^\circ\text{C}$  resulting in an ohmic contact to the back gate [39]. In the next step, we evaporate a pad of 3 nm titanium followed by 7 nm of gold on a small part ( $\sim 1 \text{ mm}^2$ ) of the top gate using a shadow mask. Making electrical contacts via standard bonding processes requires careful adjustment of the bonding parameters to avoid any damage, especially on very thin samples (see Fig. 9). On account of the small distance between the top and the back gate in this device, standard bonding processes were avoided as a precautionary measure. Instead, the electrical contacts to the gates were made by affixing the wires to the bond pads with silver paint, a method with which we reproducibly achieved good contacts.

[1] M. Kroutvar, Y. Ducommun, D. Heiss, M. Bichler, D. Schuh, G. Abstreiter, and J. J. Finley, *Nature (London)* **432**, 81 (2004).

[2] D. Press, T. D. Ladd, B. Zhang, and Y. Yamamoto, *Nature (London)* **456**, 218 (2008).

- [3] A. Greulich, A. Shabaev, D. R. Yakovlev, A. L. Efros, I. A. Yugova, D. Reuter, A. D. Wieck, and M. Bayer, *Science* **317**, 1896 (2007).
- [4] C.-Y. Lu, Y. Zhao, A. N. Vamivakas, C. Matthiesen, S. Fält, A. Badolato, and M. Atatüre, *Phys. Rev. B* **81**, 035332 (2010).
- [5] S. T. Yilmaz, P. Fallahi, and A. Imamoglu, *Phys. Rev. Lett.* **105**, 033601 (2010).
- [6] A. Greulich, S. E. Economou, S. Spatzek, D. R. Yakovlev, D. Reuter, A. D. Wieck, T. L. Reinecke, and M. Bayer, *Nat. Phys.* **5**, 262 (2009).
- [7] J. H. Prechtel, A. V. Kuhlmann, J. Houel, A. Ludwig, S. R. Valentin, A. D. Wieck, and R. J. Warburton, *Nat. Mater.* **15**, 981 (2016).
- [8] B. D. Gerardot, D. Brunner, P. A. Dalgarno, P. Öhberg, S. Seidl, M. Kroner, K. Karrai, N. G. Stoltz, P. M. Petroff, and R. J. Warburton, *Nature (London)* **451**, 451 (2008).
- [9] A. N. Vamivakas, Y. Zhao, C.-Y. Lu, and M. Atatüre, *Nat. Phys.* **5**, 198 (2009).
- [10] R. J. Warburton, *Nat. Mater.* **12**, 483 (2013).
- [11] A. V. Kuhlmann, J. H. Prechtel, J. Houel, A. Ludwig, D. Reuter, A. D. Wieck, and R. J. Warburton, *Nat. Commun.* **6**, 8204 (2015).
- [12] A. V. Kuhlmann, J. Houel, A. Ludwig, L. Greuter, D. Reuter, A. D. Wieck, M. Poggio, and R. J. Warburton, *Nat. Phys.* **9**, 570 (2013).
- [13] P. Lodahl, S. Mahmoodian, and S. Stobbe, *Rev. Mod. Phys.* **87**, 347 (2015).
- [14] I. Wilson-Rae, P. Zoller, and A. Imamoglu, *Phys. Rev. Lett.* **92**, 075507 (2004).
- [15] I. Söllner, L. Midolo, and P. Lodahl, *Phys. Rev. Lett.* **116**, 234301 (2016).
- [16] A. Javadi, I. Söllner, M. Arcari, S. L. Hansen, L. Midolo, S. Mahmoodian, G. Kiršanskė, T. Pregolato, E. H. Lee, J. D. Song, S. Stobbe, and P. Lodahl, *Nat. Commun.* **6**, 8655 (2015).
- [17] C. Reese, C. Becher, A. Imamoglu, E. Hu, B. D. Gerardot, and P. M. Petroff, *Appl. Phys. Lett.* **78**, 2279 (2001).
- [18] D. Pinotsi, P. Fallahi, J. Miguel-Sanchez, and A. Imamoglu, *IEEE J. Quantum Electron.* **47**, 1371 (2011).
- [19] P. M. Vora, A. S. Bracker, S. G. Carter, T. M. Sweeney, M. Kim, C. S. Kim, L. Yang, P. G. Brereton, S. E. Economou, and D. Gammon, *Nat. Commun.* **6**, 7665 (2015).
- [20] V. Nagavarapu, R. Jhaveri, and J. C. S. Woo, *IEEE Trans. Electron Devices* **55**, 1013 (2008).
- [21] S. E. Hosseini and M. Kamali Moghaddam, *Mater. Sci. Semicond. Process.* **30**, 56 (2015).
- [22] K. G. Lagoudakis, K. Fischer, T. Sarmiento, A. Majumdar, A. Rundquist, J. Lu, M. Bajcsy, and J. Vučković, *New J. Phys.* **15**, 113056 (2013).
- [23] A. Ludwig, J. H. Prechtel, A. V. Kuhlmann, J. Houel, S. R. Valentin, R. J. Warburton, and A. D. Wieck, *J. Cryst. Growth* **477**, 193 (2017).
- [24] L. Midolo, T. Pregolato, G. Kiršanskė, and S. Stobbe, *Nanotechnology* **26**, 484002 (2015).
- [25] J. M. Smith, P. A. Dalgarno, R. J. Warburton, A. O. Govorov, K. Karrai, B. D. Gerardot, and P. M. Petroff, *Phys. Rev. Lett.* **94**, 197402 (2005).
- [26] M. Atatüre, J. Dreiser, A. Badolato, A. Högele, K. Karrai, and A. Imamoglu, *Science* **312**, 551 (2006).
- [27] J. Dreiser, M. Atatüre, C. Galland, T. Müller, A. Badolato, and A. Imamoglu, *Phys. Rev. B* **77**, 075317 (2008).
- [28] S. G. Carter, T. M. Sweeney, M. Kim, C. S. Kim, D. Solenov, S. E. Economou, T. L. Reinecke, L. Yang, A. S. Bracker, and D. Gammon, *Nat. Photon.* **7**, 329 (2013).
- [29] R. B. Patel, A. J. Bennett, I. Farrer, C. A. Nicoll, D. A. Ritchie, and A. J. Shields, *Nat. Photon.* **4**, 632 (2010).
- [30] J. Houel, A. V. Kuhlmann, L. Greuter, F. Xue, M. Poggio, B. D. Gerardot, P. A. Dalgarno, A. Badolato, P. M. Petroff, A. Ludwig, D. Reuter, A. D. Wieck, and R. J. Warburton, *Phys. Rev. Lett.* **108**, 107401 (2012).
- [31] A. Kurzmann, A. Ludwig, A. D. Wieck, A. Lorke, and M. Geller, *Nano Lett.* **16**, 3367 (2016).
- [32] A. V. Kuhlmann, J. Houel, D. Brunner, A. Ludwig, D. Reuter, A. D. Wieck, and R. J. Warburton, *Rev. Sci. Instrum.* **84**, 073905 (2013).
- [33] R. J. Warburton, C. Schäfflein, D. Haft, F. Bickel, A. Lorke, K. Karrai, J. M. Garcia, W. Schoenfeld, and P. M. Petroff, *Nature (London)* **405**, 926 (2000).
- [34] J. J. Finley, P. W. Fry, A. D. Ashmore, A. Lemaître, A. I. Tartakovskii, R. Oulton, D. J. Mowbray, M. S. Skolnick, M. Hopkinson, P. D. Buckle, and P. A. Maksym, *Phys. Rev. B* **63**, 161305 (2001).
- [35] M. Kroner, K. M. Weiss, B. Biedermann, S. Seidl, A. W. Holleitner, A. Badolato, P. M. Petroff, P. Öhberg, R. J. Warburton, and K. Karrai, *Phys. Rev. B* **78**, 075429 (2008).
- [36] M. Kroner, K. M. Weiss, B. Biedermann, S. Seidl, S. Manus, A. W. Holleitner, A. Badolato, P. M. Petroff, B. D. Gerardot, R. J. Warburton, and K. Karrai, *Phys. Rev. Lett.* **100**, 156803 (2008).
- [37] S. Seidl, M. Kroner, P. A. Dalgarno, A. Högele, J. M. Smith, M. Ediger, B. D. Gerardot, J. M. Garcia, P. M. Petroff, K. Karrai, and R. J. Warburton, *Phys. Rev. B* **72**, 195339 (2005).
- [38] W. Lei, M. Offer, A. Lorke, C. Notthoff, C. Meier, O. Wibbelhoff, and A. D. Wieck, *Appl. Phys. Lett.* **92**, 193111 (2008).
- [39] O. Göktaş, J. Weber, J. Weis, and K. von Klitzing, *Phys. E (Amsterdam, Neth.)* **40**, 1579 (2008).